Temperature Distribution Reconstruction in Czochralski Crystal Growth Process

Javad Abdollahi, Mojtaba Izadi, and Stevan Dubljevic
Dept. of Chemical and Materials Engineering, University of Alberta, Edmonton, AB, Canada T6G 2V4

DOI 10.1002/aic.14486
Published online May 21, 2014 in Wiley Online Library (wileyonlinelibrary.com)

A mechanical geometric crystal growth model is developed to describe the crystal length and radius evolution. The crystal radius regulation is achieved by feedback linearization and accounts for parametric uncertainty in the crystal growth rate. The associated parabolic partial differential equation (PDE) model of heat conduction is considered over the time-varying crystal domain and coupled with crystal growth dynamics. An appropriately defined infinite-dimensional representation of the thermal evolution is derived considering slow time-varying process effects. The computational framework of the Galerkin's method is used for parabolic PDE order reduction and observer synthesis for temperature distribution reconstruction over the entire crystal domain. It is shown that the proposed observer can be utilized to reconstruct temperature distribution from boundary temperature measurements. The developed observer is implemented on the finite-element model of the process and demonstrates that despite parametric and geometric uncertainties present in the model, the temperature distribution is reconstructed with the high accuracy. © 2014 American Institute of Chemical Engineers *AIChE J*, 60: 2839–2852, 2014

Keywords: parabolic partial differential equation control, time-varying distributed parameter systems, temperature distribution estimation, Czochralski crystal growth process

Introduction

The Czochralski (Cz) crystal growth process is a well-known crystallization process to grow and produce single crystals. The process starts with inserting a small crystal seed into heated melt and the crystal seed is slowly drawn out of the crucible, with heated melt of crystal material, allowing the melt to solidify, and grow at the melt-crystal interface. Due to continuous and unbroken crystal lattice in single crystals, produced crystals have unique mechanical, physical, and electrical properties, which speaks for high demand for quality grown single crystals in microelectronics and optoelectronics, as well as demand for structurally robust and high temperature resistant materials.[1–3]

Due to the nature of high-tech applications reflecting in high quality of a grown crystal and high energy and time consuming growth process, there are manufacturing concerns that should be addressed in the Cz process. In particular, crystal shape and geometry, as well as crystal quality, are among the most important manufacturing concerns. The former is usually addressed by producing the crystal with constant diameter to minimize machining waste. Along the consideration of the crystal geometry from the standpoint of manufacturing, the crystal quality is also defined by physical properties of the produced crystal. Uniform composition, dopant concentration, defects density, and residual stresses in crystal are the most important properties that should be considered in a crystallization process, see [2–5].

In the Cz crystal growth process, the presence of solid and liquid phases, melt fluid flow, thermal, and heat transfer phenomena, solid–liquid interface, and pulling dynamics make the modeling and control of the Cz process a challenging task.[6,7] Due to the crystal growth and phase transition between solid and liquid phases, the crystal spatial domain undergoes time-varying changes which brings complexity to the process regulation. There are studies focusing on modeling and simulation of coupled phenomena together.[8,9] However, for control and estimation purposes and specially for model-based control/estimation, reduced order models are required. Reduced order models are used for both radius and temperature control purposes. For example, reduced order models are developed and used by Irizarry-Rivera and Seider for coupled radius and melt temperature control in the Cz crystal growth process.[10,11] In general, to achieve a simpler model description, one can apply suitable assumptions to decouple the thermal phenomena in the solid crystal and the melt for the purpose of temperature observation/control in the grown solid crystal. In particular, in this work, the temperature control and/or estimation in a solid grown crystal is formulated as a heat transfer model with interface phenomena modeled as a Dirichlet boundary condition at the melt-solid interface[12–14] (for details see Eqs. 25–27).

Real-time knowledge of temperature distribution evolution in crystal and its interfaces is necessary for monitoring and control purposes. The temperature distribution and gradients in crystal determine and influence residual stresses, crystal oxygen, and dopant concentration and grown crystal defects

Correspondence concerning this article should be addressed to S. Dubljevic at stevan.dubljevic@ualberta.ca.

concentration.[3,15] However, temperature measurements over the entire domain are not directly available and cannot be realized in practice. In particular, possibly available and realizable temperature measurement is carried out at the grown crystal boundary but cannot be used to construct the temperature and temperature gradients directly. Moreover, all the boundary temperatures are not available for direct sensor applied measurements, namely bottom boundary is the melt-crystal interface and the top is used for installing pulling devices. Usually, the only available temperature measurement is at the cylindrical surface of the crystal, and to reconstruct temperature profile over the entire domain and boundaries, an estimation strategy is required.

A boundary and in-domain state estimation/reconstruction and control strategies for parabolic partial differential equation (PDE) systems are well developed and make an active research area, see [16–18]. For example, there are several contributions on control problems with fixed spatial domain for linear PDEs,[16,17,19] nonlinear PDEs,[20–22] problems with spatially distributed actuation,[17,19,23] and boundary control problems.[20,21,24] Despite distributed parameter control strategies, state estimation algorithms for parabolic PDEs are less developed and are of interest in the context of temperature estimation in the crystal growth process. In particular, Xu et al.[25] provide a simple observer for dissipative bilinear systems with weak error convergence to zero. The Luenberger observer synthesis is used by both Vries et al.[26] for state estimation of the Sturm-Liouville systems, and Li and Xu[27] for a higher order PDE describing the rotating body-beam system. Harkort and Deutscher[28] have developed an observer-based controller framework for Riesz-spectral systems. Along the same line, Hagen et al.[29] have studied the observer and control design using spillover analysis for a class of PDEs with periodic boundary conditions. State estimation of the systems governed by parabolic PDEs on a fixed domain are well developed, however, there are limited contributions on parabolic PDEs with a moving boundary setting.

Moving boundaries and time-varying parameters bring complexity to the system that needs to be addressed in the control and estimation framework. There are several works focusing on controller design for time-varying parabolic PDEs. For example, Armaou and Christofides have reduced a 2-D heat transfer model in the Cz crystal growth process to a 1-D model, and then synthesized a controller to regulate temperature distribution in the crystal.[14] They also provided a nonoptimal stabilizing robust control law for moving boundary crystal growth problem.[30] Wang studied various optimal controller synthesis for stabilization and control of distributed systems with time-dependent spatial domains, see [31,32], while Ng and Dubljevic contributed on optimal boundary control of the Cz crystal growth process with time-varying spatial domain coupled with pulling dynamics, see [12, 33]. In the former contributions, the developed control laws require full state knowledge of the process which motivates this contribution to reconstruct the entire temperature field in the Cz process from the boundary measurement.

In the Cz process, the boundary movement is the result of the crystal growth in both radial and axial directions. The time evolution of the solid crystal determines the crystal shape and consequently, the spatial domain of the governing temperature evolution equations. The radius regulation and estimation in the Cz process have attracted several researchers. There are early works on radius regulation, for example, Gross and Kersten[34] worked on the crystal radius control and Jordan et al.[35] used the crystal weight signal as a measurement for control purposes. Recently, Winkler et al.[5,36] revisited the radius control and estimation problem, provided a modeling approach based on capillary forces and a nonlinear approach combined with a conventional PI controller to estimate and regulate the crystal radius. Neubert and Winkler[37] introduced parameters such as thermal conductivity, latent heat, average axial thermal gradients, and actual growth rate to refine the scheduling of a Proportional Integral (PI) controller for better performance. Hence, one concludes that the growth dynamics and the temperature distribution evolution in the crystal are coupled in the Cz process, however, this coupling is not taken into account in the aforementioned works.

In this article, a mechanical-geometric crystal growth model is developed based on the constant crystal growth rate, then assuming a large parametric uncertainty in the growth rate, a robust controller synthesis is provided using the input–output linearization for crystal diameter tracking. Time-varying radius and crystal length evolution, obtained from a nonlinear mechanical-geometric radius evolution model, determine the spatial domain of the underlying heat transfer model which leads to the time-varying boundary parabolic PDE model of the temperature distribution evolution which can be expressed with operators and embedded in an infinite-dimensional PDE setting. The governing temperature evolution is approximated by a time-varying parabolic PDE model on a rectangular domain and a finite-dimensional representation of the PDE model is derived using Galerkin's method. The effect of time-varying domain is investigated and is taken into account to obtain the low dimensional model. An observer is synthesized using a reduced finite-dimensional model to reconstruct the entire temperature distribution by using physically realizable temperature measurements. The separation principle is examined and shown to hold to utilize the proposed observer in the output feedback control synthesis. In addition, a finite-element method (FEM) model of the crystal growth process is used to numerically simulate the temperature evolution in the solid crystal on the nontrivial and time-varying domain. The developed FEM model is used as the actual process to evaluate and verify the performance and efficiency of the temperature reconstruction.

The temperature distribution evolution in the crystal affects the crystal quality in two ways. The first is through influencing the formation, diffusion, and aggregation of point defects and atomic oxygen in the crystal.[38] The second is through the residual stresses in the crystal that occur during crystal cooling. An accurate dynamic model of the point defects in the crystal requires the knowledge of temperature distribution over the crystal. This article focuses on the temperature estimation, and it is a basis for extending this work to control and optimization of residual stresses and point defects through manipulating the temperature distribution. The temperature control can be done to minimize the formation, diffusion, or aggregation of point defects and also to optimally control the cooling process to avoid residual stresses in the crystal.

The provided methodology for the temperature reconstruction from boundary measurements can be extended to other chemical engineering processes with time-varying domain and especially with moving front and other material processing applications with same governing equations such as Bridgman crystal growth process and/or steel slab

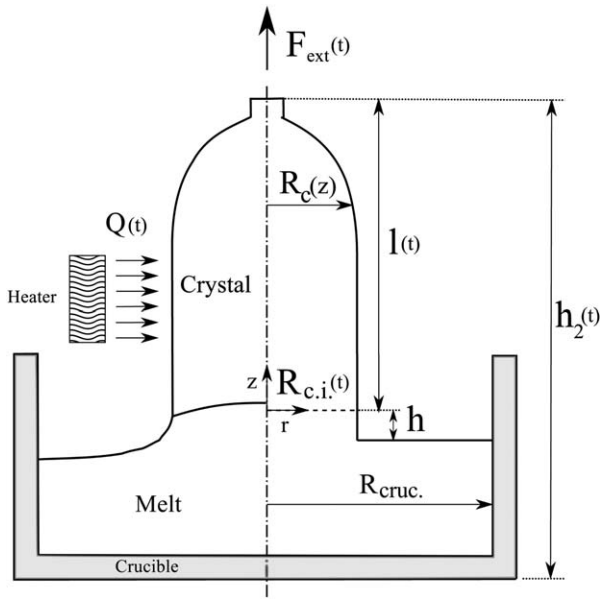

Figure 1. Schematic of the Cz crystal growth process with the realistic geometry of the process given in the left figure side, and geometric simplifications and parameters given in the right figure side.

annealing.[4,39] This article is focused on Cz crystallization process to cover more issues in practical implementation. Furthermore, the observer synthesis is developed based on reduced order Galerkin' model and finite-element model realization is provided to verify both the reduced order model and the observer. Hence that, finite-element realization is shown to be a suitable numerical approach for modeling and simulation of the Cz crystal growth process by comparing and validation of FEM results with experimental and/or numerical data carried out by different contributors.[40–43]

The organization of the article is as follow: after the Introduction, in Crystal growth model and radius regulation section, translational mechanical-geometric dynamic model for the Cz process is derived and the controller synthesis is presented to maintain constant crystal diameter in the presence of parametric uncertainty. In Heat transfer model section, the solid crystal heat transfer model is presented and the boundary conditions are defined. The infinite-dimensional PDE model representation with defined spatial operators is developed along with the model reduction using Galerkin's method and the influence of time-varying effects is described. Observer design and temperature estimation section provides the observer design, FEM model, and the implementation of the estimation strategy. Numerical simulation results are presented in Numerical simulation results section.

Crystal Growth Model and Radius Regulation

In the Cz crystal growth process, the crystal is slowly pulled out of the melt, allowing solidification of crystal at the crystal-melt interface. Mechanical pulling rate influences the crystal profile and determines the shape of the crystal. The crystal radius and growth can be regulated by a conventional Proportional Integral Derivative (PID) controller,[3,15,44,45] however, for more precise control, model-based approaches can be utilized. Model-based control approaches have attracted more attention recently, for example, Winkler and coworkers focused on nonlinear model-based control and estimation of the Cz process.[5,36,37] As for the model-based control, a sophisticated process model is required to achieve desired performance. In this work, a new approach is used for radius regulation. The influence of temperature distribution and heat transfer phenomena on crystal growth are seen as an uncertainty in the crystal growth rate. Then control synthesis is provided to compensate for large parametric uncertainty in the growth rate. The crystal growth model is derived assuming that the crystallization rate is constant, the deviation from the nominal growth rate is considered as parametric uncertainty and then the control synthesis is provided.

First principal crystal growth model

The translational movement has direct influence on the crystal surface profile and affects the crystal radius.[5] Crystal growth is modeled based on conservation of mass and Newton's second law. The schematic of the crystal pulling dynamics along with the notations are presented in Figure 1. In deriving a dynamic model, the melt-solid interface is assumed to be a horizontal plane.[46]

Assuming the same density for both the solid crystal and melt, the total volume (V_t) is constant during the process, that is

$$V_t = V_c + V_m + V_l \tag{1}$$

where V_c is the volume of the solid crystal, V_l is the melt volume, and V_m is the meniscus' volume. Eq. 1 can be written as

$$V_t = \int_0^t \pi R_{c.i.}(\tau)^2 \dot{l}(\tau) d\tau + V_m + \pi R_{cruc.}^2 (h_2(t) - l(t) - h(t)) \tag{2}$$

where $V_c = \int_0^t \pi R_{c.i.}^2 \dot{l} dt$ and $V_l = \pi R_{cruc.}^2 (h_2(t) - l(t) - h(t))$. The schematic of the crystal and crucible is shown in Figure 1. Total mass is constant and assuming a constant volume for the meniscus, then $\dot{V}_t = 0$ and mass conservation can be written as follows

$$\dot{h}_2(t) = \dot{l}(t)\left(1 - \frac{R_{c.i.}^2}{R_{cruc.}^2}\right) \tag{3}$$

where $R_{c.i.}(t)$ is the crystal radius at the interface. Conversely, the total mass subjected to motion is the crystal mass which is given as follows

$$M_c = \rho_c V_c = \rho_c \int_0^t \pi R_{c.i.}(\tau)^2 \dot{l}(\tau) d\tau \tag{4}$$

and the crystal velocity is the average of the velocity at two crystal ends and is given as

$$v_c = \dot{h}_2(t) - \dot{l}(t)/2 = \dot{l}(t)\left(\frac{1}{2} - \frac{R_{c.i.}(t)^2}{R_{cruc.}^2}\right) \tag{5}$$

applying the conservation of linear momentum (Newton's second law)

$$\frac{d(M_c v_c)}{dt} = F_{ext}(t) \tag{6}$$

and substituting Eqs. 4 and 5 into Eq. 6 results in

$$\rho_c V_c(t)\ddot{l}(t)\left(\frac{1}{2}-\frac{R_{\text{c.i.}}(t)^2}{R_{\text{cruc.}}^2}\right)+\rho_c V_c(t)\dot{l}(t)\left(\frac{-2R_{\text{c.i.}}(t)\dot{R}_{\text{c.i.}}(t)}{R_{\text{cruc.}}^2}\right)$$
$$+\rho_c\dot{l}(t)\left(\frac{1}{2}-\frac{R_{\text{c.i.}}(t)^2}{R_{\text{cruc.}}^2}\right)\dot{V}_c(t)=F_{\text{ext}}(t) \quad (7)$$

The crystal growth rate can be formulated as a function of heat fluxes in the solid–liquid interface as following[47]

$$\dot{l}(t)=\frac{\Phi_s-\Phi_l}{\pi R_{\text{c.i.}}^2\rho_c\Delta H} \quad (8)$$

Considering the constant heat flux at the interface

$$\dot{l}(t)=\frac{C_{\text{growth}}}{R_{\text{c.i.}}(t)^2} \quad (9)$$

where

$$C_{\text{growth}}=\frac{\Phi_s-\Phi_l}{\pi\rho_c\Delta H} \quad (10)$$

C_{growth} depends on the heat fluxes and material characteristics at the interface. Substituting Eq. 9 into Eq. 7 results in

$$\frac{\rho_c V_c(t)}{2}\ddot{l}(t)+\rho_c\pi C_{\text{growth}}\left(\frac{1}{2}-\frac{R_{\text{c.i.}}(t)^2}{R_{\text{cruc.}}^2}\right)\dot{l}(t)=F_{\text{ext}}(t) \quad (11)$$

Finally, in the state space form, we denote $x_1(t)=l(t)$, $x_2(t)=i(t)$, and $x_3(t)=V_c(t)$, so the model is given as

$$\begin{aligned}\dot{x}_1(t)&=x_2(t)\\ \dot{x}_2(t)&=\frac{2}{\rho_c x_3(t)}\left[F_{\text{ext}}(t)-\rho_c\pi C_{\text{growth}}\left(\frac{x_2(t)}{2}-\frac{C_{\text{growth}}}{R_{\text{cruc.}}^2}\right)\right]\\ \dot{x}_3(t)&=\pi C_{\text{growth}}\end{aligned} \quad (12)$$

and the crystal radius, $R_{\text{c.i.}}$, as the output is given as

$$R_{\text{c.i.}}(t)=\sqrt{\frac{C_{\text{growth}}}{x_2(t)}}=\sqrt{\frac{C_{\text{growth}}}{\dot{l}(t)}} \quad (13)$$

The crystal growth process starts with inserting seed crystal into the melt and, therefore, the initial condition for Eqs. 12 and 13 are the initial dimensions of the seed crystal. Specifically, the initial crystal volume is denoted by $x_3(0)=V_{c0}$.

Remark. *In the Cz crystal growth process, the Young–Laplace force acts on the solid crystal. In the above derivation of the growth dynamics of the Cz crystal growth, the Young–Laplace force is neglected. This force is usually approximated by hydrostatic force (first term) and the vertical component of the surface tension (second term),[47] is described as below*

$$F_{\text{Y.L.}}=\pi g\rho_l R_{\text{c.i.}}^2 h+\pi g\rho_l a^2 R_{\text{c.i.}}\cos(\alpha_0+\alpha_c) \quad (14)$$

where, a is the Laplace constant, α_0 and α_c are the growth and capillary angles, ρ_l is the liquid density, and g is the gravitational constant. In this work, the meniscus shape is considered to be constant, therefore, the Young–Laplace force can be calculated and incorporated into the system as a known disturbance. The crystal radius, $R_{\text{c.i.}}$, and meniscus height, h, are measured and the capillary angle can be calculated from the Young–Laplace equation[10]

$$h=a\sqrt{\frac{1-\sin(\alpha_0+\alpha_c)}{1+a/(\sqrt{2}R_{\text{c.i.}})}} \quad (15)$$

Growth control

An important objective in the Cz process is to regulate the crystal radius at a constant value along the crystal length during the process. To achieve this goal, a controller is designed based on the input–output linearization of the growth model to regulate the radius at the desired prespecified crystal radius. Assuming the pulling force as an input to the growth model and the radius of the crystal as an output, the input–output relation is obtained as

$$\frac{dR_{\text{c.i.}}}{dt}=\frac{R_{\text{c.i.}}}{2(t+V_{c0}/\pi C_{\text{growth}})}-\frac{R_{\text{c.i.}}^3}{\rho_c\pi C_{\text{growth}}^2(t+V_{c0}/\pi C_{\text{growth}})}F(t) \quad (16)$$

where $R_{\text{c.i.}}$, the crystal's radius, is the process output, $F(t)=F_{\text{ext}}(t)+\frac{\rho_c\pi C_{\text{growth}}^2}{R_{\text{cruc.}}^2}$ is the input to the growth model, V_{c0} is the crystal's initial volume. Using the input–output linearization and defining $F(t)$ as

$$F(t)=\frac{\rho\pi C_{\text{growth}}^2}{2R_{\text{c.i.}}^2}-\frac{\rho\pi C_{\text{growth}}^2(t+V_{c0}/\pi C_{\text{growth}})}{R_{\text{c.i.}}^3}u_{\text{mech.}}(t) \quad (17)$$

Equation 16 is transformed into $\dot{r}(t)=u_{\text{mech.}}(t)$. As it can be seen, the radius can be manipulated directly by $u_{\text{mech.}}(t)$. To regulate the radius at a prespecified desired constant value R_d, the control law is chosen to be $u_{\text{mech.}}(t)=-K(R_{\text{c.i.}}-R_d)$, where K is a positive number. Therefore, the following control action is derived to stabilize the process at the constant radius R_d.

$$F_{\text{ext}}(t)=\rho_c\pi C_{\text{growth}}^2\left(\frac{1}{2R_{\text{c.i.}}(t)^2}-\frac{1}{R_{\text{cruc.}}^2}\right)+K\rho\pi C_{\text{growth}}^2$$
$$\left(t+\frac{V_{c0}}{\pi C_{\text{growth}}}\right)\frac{R_{\text{c.i.}}(t)-R_d}{R_{\text{c.i.}}(t)^3} \quad (18)$$

where K is the controller gain determined in the ensuing section to compensate the parametric uncertainty in the crystal growth rate.

Modeling uncertainties and disturbance rejection

The main assumption in the mechanical modeling in the previous section is that the heat flux at the solid-melt interface is constant. However, the heat flux across the solid-melt interface changes during the process and the dominant heat transfer is the melt heat lost through the solid-melt interface. Therefore, in this section, we account for this assumption by considering a parametric uncertainty to the dynamic model given by Eq. 12. The deviation of heat flux at the solid-melt interface is considered as heat fluctuations and is defined as $d(t)$, where

$$\frac{\Phi_s-\Phi_l}{\pi\rho_c\Delta H}=C_{\text{growth}}+d(t) \quad (19)$$

The controller synthesis is based on constant heat fluxes and the deviation from this constant value results in a process model with a similar structure as given by Eq. 12. The resulting model is given as follows

$$\begin{aligned}\dot{x}_1(t)&=x_2(t)\\ \dot{x}_2(t)&=\frac{2}{\rho_c x_3(t)}\left[F_{\text{ext}}(t)-\rho_c\pi(C_{\text{growth}}+d(t))\left(\frac{x_2(t)}{2}-\frac{C_{\text{growth}}+d(t)}{R_{\text{cruc.}}^2}\right)\right]\\ \dot{x}_3(t)&=\pi(C_{\text{growth}}+d(t))\end{aligned} \tag{20}$$

$$R_{\text{c.i.}}(t)=\sqrt{(C_{\text{growth}}+d(t))/x_2(t)} \tag{21}$$

Applying the control law given by Eq. 18 to the model, Eqs. 20 and 21, result in the following relation

$$\dot{R}_{\text{c.i.}}(t)=\frac{\epsilon\ R_{\text{c.i.}}(t)}{2(t+V_{c0}/\pi(C_{\text{growth}}+d(t)))}-K(1-\epsilon)(R_{\text{c.i.}}(t)-R_{\text{d}}) \tag{22}$$

where $\varepsilon=1-\frac{C_{\text{growth}}^2}{(C_{\text{growth}}+d(t))^2}$ and $d(t)$ is the deviation from the nominal value of C_{growth}. The crystal growth rate is assumed to vary from no crystallization to fast crystallization rates and then it can be concluded that $d(t)\in(-C_{\text{growth}},\infty)$, while ϵ in Eq. 22 is $\epsilon\in(-\infty,1)$. The second term in Eq. 22 is negative for all ϵ and the first term is negative for $\epsilon\in(-\infty,0)$. For $\epsilon\in(0,1)$, the stability of the controller is guaranteed by defining K to have $\dot{R}_{\text{c.i.}}=-\mu(K)(R_{\text{c.i.}}-R_{\text{d}}(t))$. K is calculated as

$$K>\frac{\pi}{2V_{c0}C_{\text{growth}}^2}D(C_{\text{growth}}+D)(2C_{\text{growth}}+D) \tag{23}$$

where D is an upper limit for disturbance $d(t)$, $-C_{\text{growth}}<d(t)<D$.

The control law, despite the uncertainty in the crystal growth rate, stabilizes the crystal radius at the desired value. The lower bound on parametric uncertainty, $d(t)$, is $-C_{\text{growth}}$ which corresponds to no solidification in the process and it is assumed that no crystal melting happens during the process. As long as the crystallization rate is positive ($D>-C_{\text{growth}}$), the robustness of the control law suffices for regular process operation (where no melting happens). The advantage of the proposed controller is that the controller stabilizes the crystal diameter despite the uncertainty in nonmodeled thermal dynamics and effects at the crystal-melt interface. In other words, the radius control synthesis is decoupled from the phenomena that can adversely affect the crystallization rate and the radius growth.

Remark. *The crystal growth model and control strategy provided in this section is a simple and effective representation of the crystal growth dynamics used to demonstrate time-varying effects and coupling between the crystal growth and temperature distribution. However, more complex models (e.g., considering capillary forces, the meniscus dynamics, etc.) can be realized and replaced with presented model*

Heat Transfer Model

A comprehensive model of the Cz crystal growth process concerning heat conduction, fluid flow in the crucible, capillary forces at the crystal-melt interface, heat radiation, and mechanical pulling dynamics can be found in literature.[1,4,6,7] This article is concerned with the temperature distribution and heat transfer time evolution in a solid crystal as a foundation for the full state feedback control synthesis, and, therefore, domain geometry of a grown crystal is of paramount importance in modeling efforts.

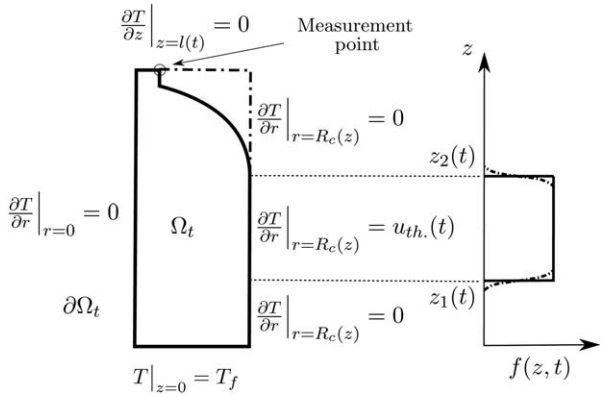

Figure 2. Geometric approximation along with the boundary conditions are given in left figure side, and the actuation profile function, $f(z,t)$ in Eq. 39, is given in right figure side.

The crystal domain evolution is determined by the crystal radius and length evolution during the process and is provided in Crystal growth model and radius regulation section. In the Cz crystal growth process, the heat transfer within the solid crystal is described by the conduction-convection PDE model given by Eq. 24, where convective terms are manifested by the growth velocity of boundaries. Figure 2 shows the process domain with simplifications made on the crystal domain along with boundary conditions. For modeling purposes, the crystal domain is assumed to be rectangular and heat transfer equations are written over the rectangular domain. Two-dimensional Cz growth process' temperature dynamics is described by the following PDE, see [1,12]

$$Pe\frac{\partial x(r,z,t)}{\partial t}=\nabla\cdot(k_r\nabla x(r,z,t))-Pe\mathbf{V}(r,z,t)\cdot\nabla x(r,z,t) \tag{24}$$

where $x(r,z,t)$ is the temperature field and ∇ is the spatial gradient operator in the cylindrical coordinate system, $Pe=\rho_c C_p v_0 R_{\text{cruc.}}/k_s$ is the Peclet number, and v_0, $R_{\text{cruc.}}$, k_s, and k_r are the nominal growth rate, crucible radius, regional thermal conductivity, and conductivity ratio, respectively and $\mathbf{V}(r,z,t)$ is the velocity vector field over the entire crystal domain. The PDE is written as an appropriately scaled time-varying moving boundary temperature model dynamics with neglected boundary velocity along the radial direction. Therefore, the temperature evolution is given by the PDE given as follows

$$\frac{\partial x}{\partial t}=\frac{1}{r}\frac{\partial}{\partial r}\left(k_0 r\frac{\partial x}{\partial r}\right)+k_0\frac{\partial^2 x}{\partial z^2}-V_z(t)\frac{\partial x}{\partial z} \tag{25}$$

where $k_0=1/Pe$ and $V_z(t)$ is the bulk movement velocity along the axial direction. The thermal conductivity ratio is equal to one for the crystal, $k_r=k_s/k_s=1$.

The boundary conditions along with the boundary actuation are shown in Figure 2. The control actuation is placed at the crystal boundary and assumed to be at a fixed height from the crucible, which means that the actuation location changes with respect to the crystal as it grows. Solidification happens at the melt-solid interface and the temperature is assumed to be the solidification temperature at this boundary. Hence that, this boundary condition at the interface decouples the heat transfer in the crystal and the melt. Moreover,

the process is axisymmetric (no flux at $r=0$) and at all other boundaries, the zero flux condition is assumed. The boundary conditions are given as

$$x\Big|_{z=0}=0; \quad \frac{\partial x}{\partial z}\Big|_{z=l(t)}=0; \quad \frac{\partial x}{\partial r}\Big|_{r=0}=0 \tag{26}$$

$$\begin{aligned}&\frac{\partial x}{\partial r}\Big|_{r=R_c(z),z<z_1(t)}=0; \quad \frac{\partial x}{\partial r}\Big|_{r=R_c(z),z>z_2(t)}=0;\\ &\frac{\partial x}{\partial r}\Big|_{r=R_c(z),z_1(t)<z<z_2(t)}=\frac{Q(t)}{Pe}=u_{\text{th.}}(t)\end{aligned} \tag{27}$$

where $R_c(z)$ and $l(t)$ are the crystal radius and length, respectively; $Q(t)$ is the heat flux from heaters; $z_1(t)$ and $z_2(t)$ indicate the spatial interval where the heater is placed, and $R_c(z)$, $l(t)$, $z_2(t)$, and $z_2(t)$ are determined from the crystal growth dynamics given by Eq. 12 and the height of the melt in crucible is given by Eq. 3. The Dirichlet boundary condition at the melt/solid interface to decouple the heat transfer in the solid crystal from the melt temperature.[12–14] The initial condition for temperature distribution $x(r,z,0)$ is the equilibrium temperature distribution over the crystal. The temperature evolution model of the grown crystal consist of a parabolic PDE model (Eq. 25) along with boundary conditions (Eqs. 26 and 27).

For temperature estimation or control purposes, one needs to consider coupled Ordinary and Partial Differential Equation (ODE-PDE) equations given by Eqs. 12 and 25–27. The coupling between ODE and PDE systems is through the PDE's spatial domain which is determined by the crystal's radius and length evolution.

Parabolic PDE model representation

Parabolic PDEs can be modeled and numerically solved by the finite-difference method (FDM) and/or FEM.[48] Despite the accuracy of numerical solutions by FDM and FEM, due to the large scale numerical realizations of these methods, they are not suitable for model-based control/estimation purposes. Spectral methods (e.g., Galerkin's method) allow parabolic PDEs to be reduced to a low-order dynamic system representation which can be easily used for control synthesis.[16] To obtain a low-order model, we utilize a general operator representation of the parabolic PDE system. In particular, the infinite-dimensional representation of a parabolic PDE on the time invariant domain can serve as basis for appropriately defined approximations on the time-varying domain within parabolic PDE representation setting. However, the use of the operators and defining Hilbert space needs to be carefully considered. The idea is to utilize already existing methods and formulations of parabolic PDEs for fixed domains, and to assure that we can consider a slow grown crystal domain evolution as a large set of well defined fixed domains that can take standard form of well defined Hilbert spaces. In particular, let $\Omega_t \in \mathbb{R}^2$ be the spatial domain of the crystal at time instance $t \in [0,T]$, and $\partial\Omega_t$ be the boundary of the domain Ω_t (rectangular boundary as shown in Figure 2). To define the appropriate basis, we define Ω as the union of all possible domains in $t \in [0,T]$ given as[13]

$$\Omega=\bigcup_{t\in[0,T]}\Omega_t\times\{t\} \tag{28}$$

Note that, Ω is a fixed open set in $\mathbb{R}^2$ with smooth boundary $\partial\Omega$ such that $\Omega_t \subset \Omega$ for all $t \in [0,T]$. Assume $\{\phi_i(\xi,t)\}$ is a family of orthonormal functions defined on a subset Ω_t for every $t \in [0,T]$ and forms a basis of $L^2(\Omega_t)$. To define a set of eigenfunctions for Ω, we define the complement of Ω_t as Ω_t^c in the fixed domain Ω, the functions $\{\phi_i(t)\}$ can be extended to the fixed domain Ω as follow

$$\phi(\xi,t)=\begin{cases}\phi(\xi) & \text{for } \xi\in\Omega_t,\\ 0 & \text{for } \xi\in\Omega_t^c\end{cases} \tag{29}$$

where Ω_t^c is the complement of Ω_t in Ω. The inner product on $L^2(\Omega)$, is defined as

$$\begin{aligned}\langle\phi(t),\psi(t)\rangle_{L^2(\Omega)}&=\int_\Omega\phi(\xi,t)\psi(\xi,t)d\xi\\ &=\int_{\Omega_t}\phi(\xi)\psi(\xi)d\xi=\langle\phi(t),\psi(t)\rangle_{L^2(\Omega_t)}\end{aligned} \tag{30}$$

Implementing the formulation given by Eqs. 28–30, the parabolic PDE model, given by Eq. 25, along with boundary conditions, given by Eqs. 26 and 27, is written in the state space formulation on a fixed domain following the formulation given by Ref. 16 as

$$\frac{\partial x(t)}{\partial t}=\mathfrak{A}(t)x(t) \tag{31}$$

$$\mathfrak{B}(t)x(t)=[0,u_{\text{th.}}(t),0]^T \tag{32}$$

where $x(t) \in L^2(\Omega)$ is the state of the system. The operator $\mathfrak{A}(t)$ is given by

$$\mathfrak{A}(t)=\frac{1}{r}\frac{\partial}{\partial r}\left(k_0 r\frac{\partial}{\partial r}\right)+k_0\frac{\partial^2}{\partial z^2}-V_z(t)\frac{\partial}{\partial z} \tag{33}$$

with the domain

$$D(\mathfrak{A}(\mathscr{T}))=\Big\{\phi\in L^2(\Omega):\phi,\frac{\partial\phi}{\partial z},\frac{\partial\phi}{\partial r}\text{ are a.c.and }\mathfrak{A}(t)\phi\in L^2(\Omega), \tag{34}$$

$$\phi(r,0,t)=0,\ \frac{\partial\phi}{\partial r}(0,z,t)=0,\frac{\partial\phi}{\partial r}(r,l(t),t)=0\Big\}$$

where a.c. means absolutely continuous, $l(t)$ and $R_c(z)$ are the crystal length and radius, respectively. The boundary operator $\mathfrak{B}(t):L^2(\Omega)\to\mathbb{R}^3$ represents the boundary conditions in Eq. 27 and is given by

$$\mathfrak{B}(t)\phi=\begin{bmatrix}\frac{\partial\phi}{\partial r}|_{r=R_c(z),z<z_1(t)}\\ \frac{\partial\phi}{\partial r}|_{r=R_c(z),z>z_2(t)}\\ \frac{\partial\phi}{\partial r}|_{r=R_c(z),z_1(t)<z<z_2(t)}\end{bmatrix} \tag{35}$$

The transformation, $p(t)=x(t)-b(r,z,t)u_{\text{th.}}(t)$, with function $b(r,z,t)$ satisfying,

$$\mathfrak{B}(t)b(r,z,t)u_{\text{th.}}(t)=[0,u_{\text{th.}}(t),0]^T \tag{36}$$

transfers the PDE model, Eqs. 25–27, to the following PDE with in-domain actuation

$$\frac{dp(t)}{dt}=\mathcal{A}p(t)+\mathcal{A}b(t)u_{\text{th.}}(t)-b(t)\dot{u}_{\text{th.}}(t)-\dot{b}(t)u_{\text{th.}}(t) \tag{37}$$

where the new $\mathcal{A}(t)$ operator is defined as

$$\mathcal{A}(t)=\frac{1}{r}\frac{\partial}{\partial r}\left(k_0 r\frac{\partial}{\partial r}\right)+k_0\frac{\partial^2}{\partial z^2}-V_z(t)\frac{\partial}{\partial z} \tag{38}$$

with the domain $D(\mathcal{A}(t))=D(\mathfrak{A}(t))\cap\ker\ \mathfrak{B}(t)$.

The spatial actuation profile function $b(r,z,t)$ satisfying Eq. 36 is not unique and it only requires to satisfy Eq. 36. In this work, $b(r,z,t)$ is considered as the following function

$$b(r,z,t)=\frac{r^2}{2R_{\text{c.i.}}(t)}f(z,t)+\frac{z^2-2l(t)z}{l(t)^2} \tag{39}$$

In Eq. 39, $R_{\text{c.i.}}(t)$ and $l(t)$ are time-varying and are determined by the growth dynamics, from Eqs. 12, while $f(z,t)$ is the actuation profile at the boundary in axial direction, which indicates the interval that reflects input flux to the system (see Figure 2).

Low dimensional model

The PDE represented by Eq. 25 along with boundary conditions in Eqs. 26 and 27 is transformed into Eq. 37 using the transformation $x(t)=p(t)+b(r,z,t)u_{\text{th.}}(t)$. To reduce the infinite-dimensional representation of the process to a finite-dimensional model, Galerkin's method is used where only a finite number of eigenfunctions is used to describe the PDE state.

The eigenvalue problem, $\mathcal{A}(t)\Phi=\lambda(t)\Phi$, is considered with homogenous boundary conditions

$$\Phi(0,r,t)=0;\ \frac{\partial\Phi}{\partial z}|_{z=l(t)}=0$$
$$\frac{\partial\Phi}{\partial r}|_{r=0}=0;\ \frac{\partial\Phi}{\partial r}|_{r=\text{Rc}(t)}=0$$

Solving the eigenvalue problem for the radial and axial directions yield to a family of time-parametrized eigenfunctions, $\phi_m(z,t),\psi_n(r,t)$

$$\phi_m(z,t)=\left(\frac{l(t)}{2}-\frac{\sin(2\alpha_m l(t))}{4\alpha_m}\right)e^{\frac{V_z(t)z}{2k_0}}\sin(\alpha_m z) \tag{40}$$

where α_m is the mth root of the transcendental equation

$$\tan(\alpha_m l(t))=-\frac{2k_0}{V_z}\alpha_m \tag{41}$$

and,

$$\psi_n(r,t)=\frac{\sqrt{2}}{Rc(t)J_0(\beta_n)}J_0(\beta_n r/Rc(t)) \tag{42}$$

where $J_0(r)$ is the Bessel function of the first kind and zero order, and β_n is the nth root of the $J_1(\beta_n)=0$. The corresponding eigenvalues are

$$\lambda_{mn}(t)=-k_0(\alpha_m^2+\beta_n^2)-\frac{1}{2}k_0^{-1}\frac{V_z(t)^2}{2} \tag{43}$$

with corresponding functions

$$\Phi_{mn}(r,z,t)=\phi_m(z,t)\psi_n(r,t) \tag{44}$$

The weighted norm over the spatial domain is defined as

$$\langle\phi_i,\psi_j\rangle_\sigma=\int_\Omega\phi_i(z,t)\psi_j(r,t)\sigma(r,z,t)d\Omega \tag{45}$$

where $\sigma(r,z,t)$ is defined as

$$\sigma(r,z,t)=\sigma_r(r)\sigma_z(z)=re^{-\frac{V_z(t)}{k}z} \tag{46}$$

such that the operator is self-adjoint with respect to $\sigma(r,z,t)$.

Then, from Eq. 37, we can obtain an extended state space system, with state $p^e(t)=[u_{th.}(t),p(t)^T]^T$, on the extended Hilbert space, $H^e=H\oplus R$ which leads to the following time-varying boundary control problem

$$\frac{dp^e(t)}{dt}=\begin{bmatrix}0 & 0\\ \mathcal{A}(t)b(t)-\dot{b}(t) & \Lambda(t)+\Delta(t)\end{bmatrix}\begin{bmatrix}u_{\text{th.}}(t)\\ p(t)\end{bmatrix}+\begin{bmatrix}1\\ -b(t)\end{bmatrix}\tilde{u}_{\text{th.}}(t)=A^e(t)p^e(t)+B^e(t)\tilde{u}_{\text{th.}}(t) \tag{47}$$

$$y=T(r,z,t)=C^e(t)p^e \tag{48}$$

where $p^e=[u_{\text{th.}}(t)\ p^T]^T$ is the extended state, $\tilde{u}_{\text{th.}}(t)=\dot{u}_{\text{th.}}(t)$, $\Lambda(t)$ is associated with the eigenvalues of $\mathcal{A}(t)$ and $\Delta(t)$ is associated with the time-varying effects of the eigenfunctions. $y=T(r,z,t)$ is the system output, where $C^e(t)$ is the output operator which denotes the output measurements. $\Delta(t)$ is expressed as follows

$$\Delta(i,j)=\langle\Phi_i,\frac{\partial\Phi_j}{\partial t}\rangle_\sigma \tag{49}$$

Equation 47 is the infinite-dimensional representation of the parabolic PDE of Eq. 37, accounting for the time-varying domain geometry. The process model in Eq. 47 has eigenvalues given by the $\Lambda(t)$ which may be perturbed by $\Delta(t)$ terms evolution. Therefore, the time-varying domain effects, $\Delta(t)$, can influence diagonal matrix $\Lambda(t)$. In the next section, it is demonstrated that the matrix $\Delta(t)$ is diagonal with negative entries implying that the time-varying domain will not destabilize the system. From Eq. 47, one concludes that the process is driven by the derivative of input and through the boundary actuation transformation $b(t)$.

Effect of time-varying domain

It can be shown that the effects of the time-varying domain result in off-diagonal terms evolution given in Eqs. 47–49. Careful inspection of the inner product in Eq. 49 reveals that after a finite-time passed, the off-diagonal terms will vanish. To calculate $\langle\Phi_i,\frac{\partial\Phi_j}{\partial t}\rangle_\sigma$, assume, $\Phi_i(r,z,t)=\phi_m(z,t)\psi_n(r,t)$ and $\Phi_j(r,z,t)=\phi_q(z,t)\psi_s(r,t)$, where m,n,q,s are integer numbers according to Eq. 44. $\Delta(i,j)$ given by Eq. 47 is written as

$$\Delta(i,j)=\langle\Phi_i,\frac{\partial\Phi_j}{\partial t}\rangle_\sigma=\langle\phi_m,\phi_q\rangle_{\sigma_z}\langle\psi_n,\frac{\partial\psi_s}{\partial t}\rangle_{\sigma_r}+\langle\phi_m,\frac{\partial\phi_q}{\partial t}\rangle_{\sigma_z}\langle\psi_n,\psi_s\rangle_{\sigma_r} \tag{50}$$

The eigenfunctions in each direction (radial or axial) are orthonormal and then the inner product in Eq. 50 can be written as

$$\Delta(i,j)=\begin{cases}0 & \text{if } m\neq q \ \&\ n\neq s\\ \langle\psi_n,\frac{\partial\psi_s}{\partial t}\rangle_{\sigma_r} & \text{if } m=q \ \&\ n\neq s\\ \langle\phi_m,\frac{\partial\phi_q}{\partial t}\rangle_{\sigma_z} & \text{if } m\neq q \ \&\ n=s\\ \langle\phi_m,\frac{\partial\phi_q}{\partial t}\rangle_{\sigma_z}+\langle\psi_n,\frac{\partial\psi_s}{\partial t}\rangle_{\sigma_r} & \text{if } m=q \ \&\ n=s\end{cases} \tag{51}$$

To explore the influence of the terms contained in $\Delta(t)$ on the model dynamics given by Eq. 47, the eigenfunctions are investigated. Namely, in the case when the radius controller provided in Eq. 18 stabilizes the crystal at a desired constant radius such that it can be assumed that $\dot{R}_{\text{c.i.}}(t)\to 0$, and

which leads according to Eq. 13, to the constant crystal growth rate $\dot{l}(t)$. Consequently, the constant crystal radius in Eq. 42 results in time-invariant eigenfunctions in radial direction such that

$$\left\langle \psi_n, \frac{\partial \psi_s}{\partial t} \right\rangle_{\sigma_r} = 0 \tag{52}$$

To calculate the remaining terms in Eq. 51, the roots of Eq. 41 are approximated by $\alpha_m = \frac{1}{l(t)}(m\pi - \frac{\pi}{2})$ (see Figure 3). The eigenfunctions in Eq. 40 can then be simplified as

$$\phi_m(z,t) = \frac{l(t)}{2} e^{\frac{V_z(t)z}{2k_0}} \sin(\alpha_m z) \tag{53}$$

and the remaining term in Eq. 51, $\langle \phi_m, \frac{\partial \phi_q}{\partial t} \rangle_{\sigma_z}$, is calculated analytically as follows

$$\langle \phi_m, \frac{\partial \phi_q}{\partial t} \rangle_{\sigma^z} = \frac{1}{2} V_z(t) \int_0^{l(t)} \sin(\alpha_m z) \sin(\alpha_q z) dz + \frac{1}{2} l(t) \dot{\alpha}_q(t) \int_0^{l(t)} \sin(\alpha_m z) \cos(\alpha_q z) z dz \tag{54}$$

which leads o

$$\langle \phi_m, \frac{\partial \phi_q}{\partial t} \rangle_{\sigma_r} = -\frac{V_z(t) l(t)}{8} \delta_{mq} \tag{55}$$

where, $l(t)$ and $V_z(t)$ are crystal length and pulling velocity, respectively, and δ_{mq} is the Kronecker delta. The time-varying effect represented by $\Delta(i,j)$ is reduced to a diagonal matrix using Eqs. 51–55 and the eigenvalues of the system represented in Eq. 47, $\lambda_i^e(t)$ can be expressed as $\lambda_i^e(t) = \lambda_i(t) - \frac{V_z(t) l(t)}{8}$. This diagonal form of the infinite-dimensional representation of temperature dynamics allows for decoupling between slow and fast modal states and provides a basis for model reduction of dissipative systems represented by parabolic PDEs. In other words, a few slow modes can be chosen to model the temperature dynamics with high accuracy.

Observer Design and Temperature Estimation

The finite-dimensional representation of the temperature dynamics, given by Eq. 47, is used for temperature estimation. Temperature measurements are available at crystal boundaries and can be used to reconstruct the temperature field over the entire domain using a few most dominant and slow modes.

It can be shown that point temperature measurements at boundary with the Neumann boundary condition is enough for the entire temperature profile reconstruction. Assume the measurements are carried out at point (r^*, z^*). Then the temperature measurement, $x(r^*, z^*, t)$, can be written as follows

$$x(r^*, z^*, t) = b(r^*, z^*, t) u_{th.}(t) + \sum_{i=1}^{\infty} p_i \Phi_i(r^*, z^*, t) = C^e(t) p^e(t) \tag{56}$$

where $b(r^*, z^*, t)$ is the boundary transformation function in Eq. 39, $u_{\text{th.}}(t)$ is the heat flux input, p_i is the ith mode, $\Phi_i(r^*, z^*, t)$ is the ith eigenfunction evaluated at the measurement point, $p^e(t)$ is the extended state vector, and $C^e(t)$ is the output operator defined as follow

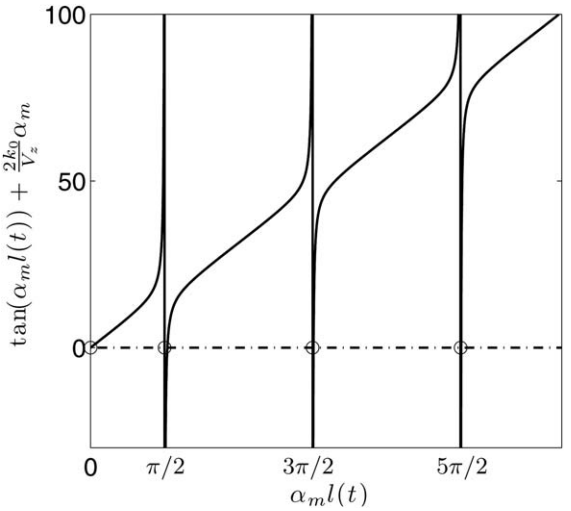

Figure 3. Roots of Eq. 41 are shown to be approximated by $m\pi - \frac{\pi}{2}$.

$$C^e(t) = [b(r^*, z^*, t),\ \Phi_1(r^*, z^*, t),\ \Phi_2(r^*, z^*, t), \ldots] \tag{57}$$

Since the input $u_{\text{th.}}(t)$ is known, the approximate observability matrix, $\mathcal{O}^{N+1} = [C^{eT}, A^{eT} C^{eT}, \ldots]^T$, for the system given by Eq. 47, for the first N modes is reduced and can be expressed as Eq. 58. Note that, as $u_{\text{th.}}(t)$ is known and measurable, rank $(\mathcal{O}^{N+1}) = \text{rank}\,(\mathcal{O}^N) + 1$

$$\mathcal{O}^N = [C^T, A^T C^T, \ldots, A^{N-1T} C^T]^T \tag{58}$$

where $C = [\Phi_1, \Phi_2, \ldots, \Phi_N]_{(r^*, z^*, t)}$ and $A = \Lambda(t) - \frac{V_z(t) l(t)}{8} I$. Using a linear transformation, the matrix $\mathcal{O}^N$ can be transformed into $[C^T, \Lambda^T C^T, \ldots, \Lambda^{N-1T} C^T]^T$ which has the same rank as $\mathcal{O}^N$

$$rank(\mathcal{O}^N) = rank \begin{pmatrix} \Phi_1 & \Phi_2 & \ldots & \Phi_N \\ \lambda_1 \Phi_1 & \lambda_2 \Phi_2 & \ldots & \lambda_1 \Phi_N \\ \vdots & \vdots & \ddots & \vdots \\ \lambda_1^{N-1} \Phi_1 & \lambda_2^{N-1} \Phi_2 & \ldots & \lambda_1^{N-1} \Phi_N \end{pmatrix}_{(r^*, z^*, t)}$$

The observability matrix is full rank if the eigenvalues do not vanish at the measurement point. Therefore, a single measurement at the boundary with the Neumann condition will suffice to satisfy the approximate observability condition. Note that the observability matrix for the parabolic PDE with time-varying domain reduces to the standard approximate observability matrix (see [49]).

To accomplish model order reduction, modal decomposition is used to model the parabolic PDE, given by Eq. 24, and reduce the temperature evolution to a low dimensional ODE. As expected in the case of parabolic PDEs, the few most dominant modes of the system can reconstruct the temperature profile with high accuracy. Furthermore, a Luenberger observer is used to estimate the most dominant modes and to reconstruct the temperature profile. To make relevant comparison with our findings, we also develop a high fidelity FEM model of the crystal growth PDE as our plant. The FEM model is constructed on the realistic and noncylindrical crystal geometry with boundary actuation. A mesh moving scheme is utilized to discretize the time-varying domain to

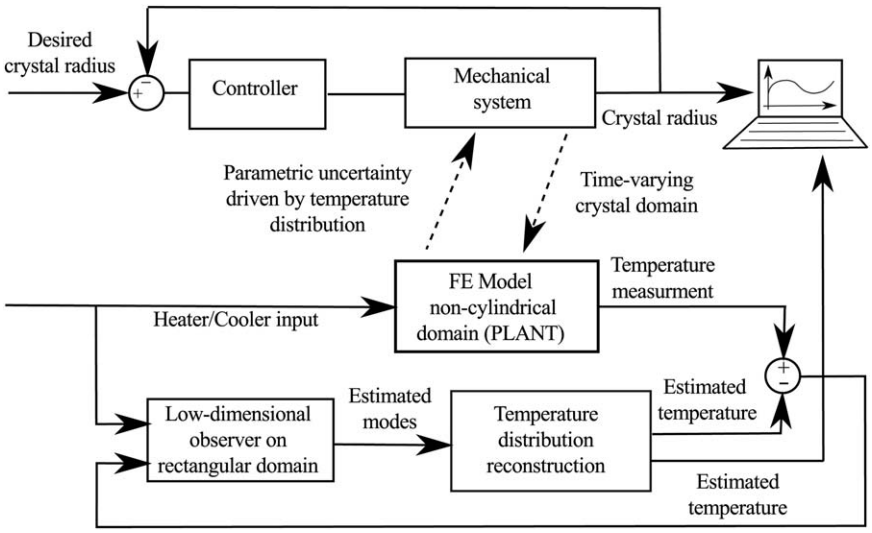

Figure 4. Temperature distribution reconstruction algorithm and the coupling between crystal growth and temperature dynamics.

develop the FEM model of the process. A point measurement is used for the state reconstruction and is taken at the crystal boundary (shown in Figure 2). In our simulation studies and analysis temperature measurement from the FEM model is fed back to the observer and the temperature distribution is reconstructed. The estimation strategy is shown in Figure 4. The Luenberger observer is utilized given as follow

$$\frac{d\hat{p}^e(t)}{dt}=A^e(t)\hat{p}^e(t)+B^e(t)\tilde{u}_{\text{th.}}(t)+L(t)(y(t)-\hat{y}(t)\ ) \tag{59}$$

where $A^e(t), B^e(t)$ are given in Eq. 47. $L(t)$ is the observer gain and is evaluated at each time step to place the eigenvalues of the error dynamics, $A^e(t)-L(t)C^e(t)$, at prespecified values.

The proposed observer estimates the temperature distribution evolution in grown crystal and to utilize the reconstructed temperature distribution for feedback control purposes, we need to explore the separation principle to ensure the stability of the closed loop process when output regulation—which includes the gain-based feedback and observer—is used. We assume that there exists a stabilizing control law $u_{\text{th.}}(t)=-Fp(t)$ for the temperature distribution model, given by

$$\frac{d}{dt}\begin{pmatrix}u_{\text{th.}}(t)\\ p(t)\end{pmatrix}=\begin{pmatrix}0 & 0\\ \mathfrak{A}(t)\mathcal{B}(t) & \mathcal{A}(t)\end{pmatrix}\begin{pmatrix}u_{\text{th.}}(t)\\ p(t)\end{pmatrix}+\begin{pmatrix}I\\ -\mathcal{B}(t)\end{pmatrix}\tilde{u}_{\text{th.}}(t) \tag{60}$$

$$y=T(r,z,t)=(\mathcal{C}(t)\mathcal{B}(t)\ \ \mathcal{C}(t))\begin{pmatrix}u_{\text{th.}}(t)\\ p(t)\end{pmatrix} \tag{61}$$

where $\mathfrak{A}(t)$, $\mathcal{A}(t)$, $\mathcal{B}(t)$, and $\mathcal{C}(t)$ are the operators introduced in Parabolic PDE model representation section. The proposed temperature estimation in Eq. 59 is written as

$$\frac{d\hat{p}(t)}{dt}=\mathcal{A}\hat{p}(t)+\mathfrak{A}\mathcal{B}u_{\text{th.}}(t)-\mathcal{B}\tilde{u}_{\text{th.}}(t)+L(t)(y(t)-\mathcal{C}\hat{p}(t)-\mathcal{C}\mathcal{B}u_{\text{th.}}(t)) \tag{62}$$

the time notation is not shown for a simpler representation. Substituting $u_{\text{th.}}(t)=-F\hat{p}(t)$, the actual and estimated modes are given by

$$\frac{dp(t)}{dt}=\mathcal{A}p(t)-\mathfrak{A}\mathcal{B}F\hat{p}(t)+\mathcal{B}F\dot{\hat{p}}(t) \tag{63}$$

$$\frac{d\hat{p}(t)}{dt}=\mathcal{A}\hat{p}(t)-\mathfrak{A}\mathcal{B}F\hat{p}(t)+\mathcal{B}F\dot{\hat{p}}(t)+L\mathcal{C}(p(t)-\hat{p}(t)) \tag{64}$$

Assuming the error $e(t)=p(t)-\hat{p}(t)$, Eqs. 63 and 64 can be written as

$$[I-BF]\dot{\hat{p}}\ (t)=[\mathcal{A}-\mathfrak{A}\mathcal{B}F]\hat{p}(t)+L\mathcal{C}e(t)\dot{e}(t)=[\mathcal{A}-L\mathcal{C}]e(t)$$

or alternatively as

$$\dot{p}(t)=\Gamma^{-1}[\mathcal{A}-\mathfrak{A}\mathcal{B}F]p(t)+[(I-\Gamma^{-1})(\mathcal{A}-L\mathcal{C})+\Gamma^{-1}\mathfrak{A}\mathcal{B}F]e(t)$$
$$\dot{e}(t)=[\mathcal{A}-L\mathcal{C}]e(t)$$

where $\Gamma=(I-\mathcal{B}F)$. The unified closed loop system is given by

$$\begin{pmatrix}\dot{p}(t)\\ \dot{e}(t)\end{pmatrix}=\begin{pmatrix}\Gamma^{-1}(\mathcal{A}-\mathfrak{A}\mathcal{B}F) & (I-\Gamma^{-1})(\mathcal{A}-L\mathcal{C})+\Gamma^{-1}\mathfrak{A}\mathcal{B}F\\ 0 & \mathcal{A}-L\mathcal{C}\end{pmatrix}\begin{pmatrix}p(t)\\ e(t)\end{pmatrix} \tag{65}$$

The operators $\mathcal{A}$ and $\mathfrak{A}$ are identical operators with different domains, however, $D(\mathcal{A})\subset D(\mathfrak{A})$ and Eq. 65 can be written as

$$\begin{pmatrix}\dot{p}(t)\\ \dot{e}(t)\end{pmatrix}=\begin{pmatrix}\Gamma^{-1}\mathcal{A}\Gamma & (I-\Gamma^{-1})(\mathcal{A}-L\mathcal{C})+\Gamma^{-1}\mathfrak{A}\mathcal{B}F\\ 0 & \mathcal{A}-L\mathcal{C}\end{pmatrix}\begin{pmatrix}p(t)\\ e(t)\end{pmatrix}=\mathbb{A}\begin{pmatrix}p(t)\\ e(t)\end{pmatrix} \tag{66}$$

where the eigenvalues of the unified system, $\mathbb{A}$, are given as $\sigma(\mathbb{A})=\sigma(\Gamma^{-1}\mathcal{A}\Gamma)\cup\sigma(\mathcal{A}-L\mathcal{C})$. Γ is assumed to be invertible and, therefore, $\sigma(\mathbb{A})=\sigma(\mathcal{A})\cup\sigma(\mathcal{A}-L\mathcal{C})$. Since the operator $\mathcal{A}$ is stable and the eigenvalues of $\mathcal{A}-L\mathcal{C}$ are placed at prespecified locations, the unified closed loop system of control and state estimation, Eq. 66, is stable and the separation principle holds. It is concluded that the proposed observer can be utilized for state reconstruction in output feedback regulation frameworks.

Table 1. Physical and Numerical Parameters

Parameter	Value	Dimensionless Value
Solidification temperature, T_s	1430°C	0
Crystal density, ρ_c	2420 kg/m^3	–
Scaled conductivity, k_0	–	0.025
Peclet number, Pe	–	0.1
Time scale	87 min	1
Sampling time	1 samples/min	0.01
Spatial discretization	–	40,100
Nominal crystal growth rate	5 cm/h	–
ODE controller gain, K	0.005	–
Crucible radius, $R_{cruc.}$	7.3 cm	1
Initial crystal radius	3.5 cm	0.48
Desired crystal radius	5 cm	0.68
Initial crystal length	7.3 cm	1

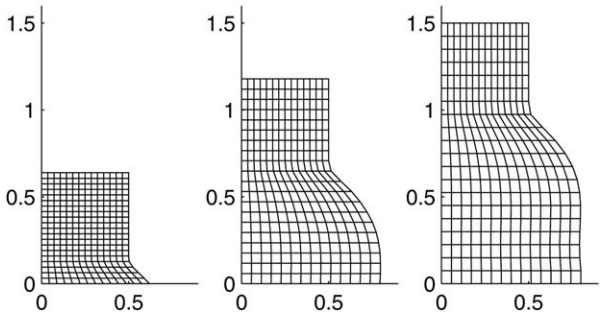

Figure 5. Moving mesh used for FE analysis.

Numerical Simulation Results

The proposed radius control and temperature reconstruction is simulated numerically and is validated by implementing on a FEM model of the process (see Figure 4). The considerations regarding numerical implementation and results of radius control and temperature reconstruction are explained in the following paragraphs. The parameters used for numerical simulation are presented in Table 1.

The FEM model of heat conduction in the crystal with noncylindrical and time-varying domain is utilized as the plant in numerical simulations. The crystal domain movement is obtained from crystal radius and length evolution dynamics, Eqs. 20 and 21, and a mesh moving scheme is utilized to discretize the time-varying geometry of the domain in developing the finite-element model of the process. Due to the fact that the evolution of the crystal domain is known from the crystal growth dynamics, the Arbitrary Lagrangian Eulerian method[48] is used to spatially discretize the domain of interest as shown in Figure 5. The finite-element mesh consists of 10×20 two-dimensional linear 4-node elements which discretizes spatial geometry to 220 degrees of freedom. The evolution of the time-dependent set of ordinary differential equations obtained from the finite-element model is realized by first-order implicit time integration with the time step $dt = 0.01$.

The parabolic PDE, Eq. 25, is represented by a finite-dimensional model, Eq. 37, using computational framework of the Galerkin's method. The Galerkin's method on a fixed domain is a well-known method for order reduction of parabolic PDE equations, but in the case of a time-varying domain, few considerations should be taken into account. Temperature distribution evolution in growing crystal is represented by evolution of both the spectral modes, $p(t)$, and the basis eigenfunctions, $\Phi_i(r,z,t)$. Hence, due to the time-varying nature of the process, the basis eigenfunctions, obtained from eigenvalue problem, will be also time-varying. To integrate the modes in time and calculate the modes and temperature distribution evolution, the modes evolution are calculated on a fixed domain and then the resulting temperature distribution is mapped into the time evolved new geometry; then the modes are recalculated by simple projection on the new evolved geometry configuration. The algorithm used for numerical implementation of the Galerkin's method on the time-varying domain is given by Table 2. The geometry and temperature mappings between different domain configurations are carried out using a property preserving transformation which preserves the total thermal energy over the domain. The domain configuration is obtained from the crystal radius and length evolution. For a slow time-varying process, the geometry mapping between different domain configurations, $\mathcal{T} : (r,z) \in \Omega_{t_0} \rightarrow (\hat{r},\hat{z}) \in \Omega_t$, is assumed to be smooth and invertible and consequently, the temperature transformation is given as, $T_{\Omega_t}(r,z) = J^{-1} T_{\Omega_{t_0}}(r,z)$, where J^{-1} is the determinant of the inverse of the Jacobian matrix, $J = \partial(r,z)/\partial(\hat{r},\hat{z})$.[50]

As the heat flux is provided through an interval on the boundary, the actuation structure is described by a step function in the z direction, see Figure 2. This function is smoothed out using the sigmoid function to avoid discontinuity when transforming the temperature profile using the transformation $x(t) = p(t) + b(r,z,t)u_t h(t)$. Using the step-like function for actuation and boundary conditions, avoids the Neumann and Dirichlet boundary condition mismatch at corner points. Moreover, as aforementioned, the Galerkin decomposition and reduction of the PDE is carried out with the assumption that the domain is rectangular and the radius variation along the crystal is ignored.

In the Galerkin's method, the low dimensional model with twelve dominant modes is used for temperature simulation. Figure 6 shows the obtained first three eigenvalues using Galerkin's method compared to the most dominant eigenvalues of the finite-element analysis. As it can be seen, the

Table 2. Numerical Algorithm for Implementation of Galerkin's Method on Time-Varying Domain

$t=t_0$:	$p_i(t_0) = \langle T_{\Omega_{t_0}}(r,z,t_0), \Phi_i(r,z,t_0) \rangle$	Obtain the modes at t_0 on domain Ω_{t_0} by projecting temperature on $\Phi_i(r,z,t_0)$.
	$p^e(t_0+\Delta t) = p^e(t_0) + (A^e(t_0)p^e(t_0) + B^e(t_0)\tilde{u}_{th.}(t_0))\Delta t$	Evolve the modes in time on domain configuration Ω_{t_0}.
	$T^{aux}_{\Omega_{t_0}}(r,z,t_0+\Delta t) = \sum_{i=1}^{N} p_i(t_0+\Delta t)\Phi_i(r,z,t_0)$	Obtain temperature distribution calculated on domain Ω_{t_0} using evolved modes.
	$\mathcal{T} : (r,z) \in \Omega_{t_0} \rightarrow (\hat{r},\hat{z}) \in \Omega_{t_0+\Delta t}$	Obtain new domain configuration from growth dynamics.
	$T_{\Omega_{t_0+\Delta t}}(r,z,t_0+\Delta t) = J^{-1} T^{aux}_{\Omega_{t_0}}(r,z,t_0+\Delta t)$	Map the temperature distribution to new domain configuration $\Omega_{t_0+\Delta t}$.
$t=t_0+\Delta t$:	$p_i(t_0+\Delta t) = \langle T_{\Omega_{t_0+\Delta t}}(r,z,t_0+\Delta t), \Phi_i(r,z,t_0+\Delta t) \rangle$	Obtain the modes at $t_0+\Delta t$ on domain configuration $\Omega_{t_0+\Delta t}$ by projecting temperature on $\Phi_i(r,z,t_0+\Delta t)$

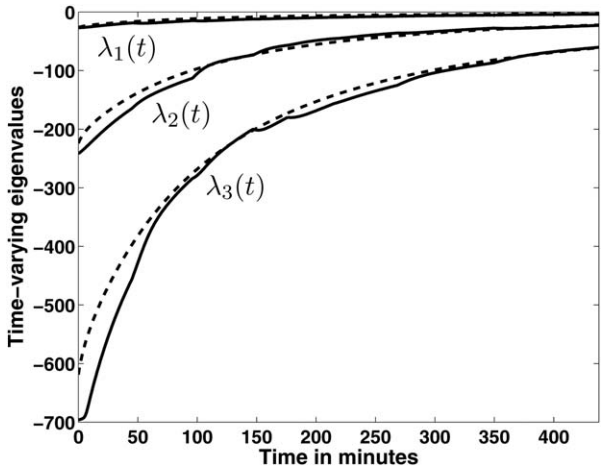

Figure 6. Time evolution of the most dominant eigenvalues in Galerkin method (dashed lines) compared to the few slowest eigenvalues of evolution matrix in finite-element analysis (solid lines).

time-varying behavior of eigenvalues are close enough to represent the model by the Galerkin's method. It can be inferred that refining the mesh size in FEM will decrease

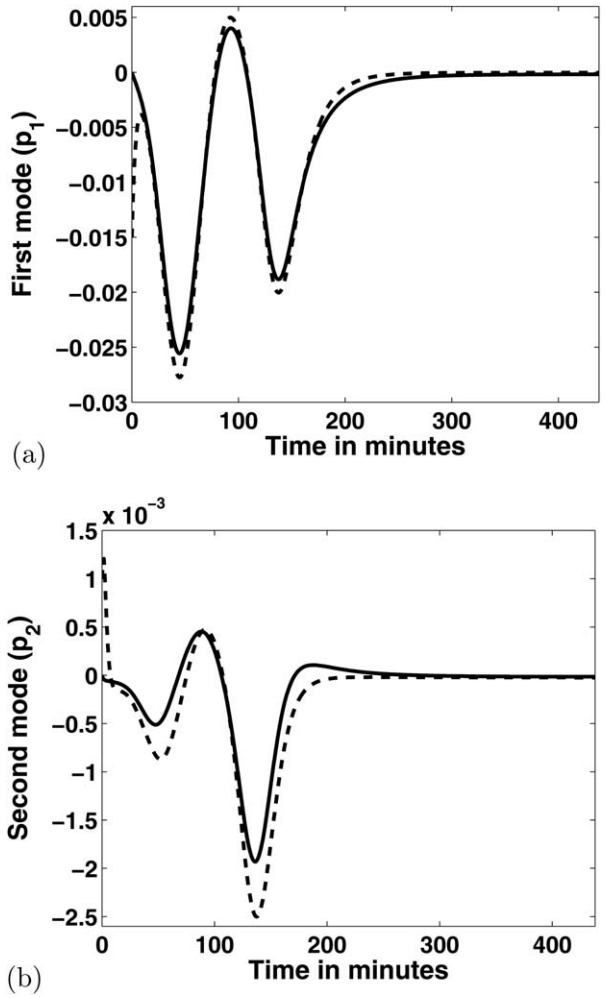

Figure 7. Estimated modes (dashed lines) compared to the actual modes (solid lines) for first two modes of the temperature evolution system.

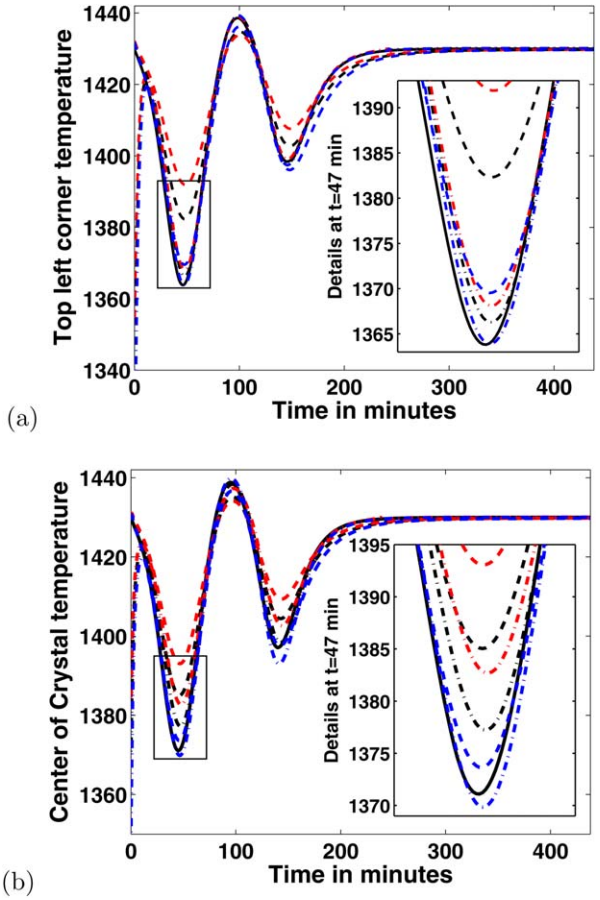

Figure 8. Estimated temperature at crystal boundary (a) and an in-domain point (b) - Solid lines represent the FEM results, open loop simulation results from Galerkin's method are presented by dashed lines, while dash-dotted lines show the estimated temperatures.

Black lines represent the case with no mismatch in crystal radius in the FEM and the observer model, blue and red lines demonstrate the case with smaller and larger crystal radius in the observer model than the FEM, respectively. [Color figure can be viewed in the online issue, which is available at wileyonlinelibrary.com.]

the deviation between eigenvalues obtained from these methods.

The estimation is carried out through the estimation of the dominant modes using reduced order model of temperature evolution dynamics. The number of modes to be used in temperature estimation is determined by the accuracy of the estimation and a minimum number of the modes is chosen. The first two dominant modes are used for temperature reconstruction. Hence, using in estimation more than two modes does not significantly increases the estimation accuracy. The estimated modes (dashed lines) along with the actual modes obtained from reduced order model (solid lines) are shown in Figure 7. Further, the estimated temperature at two different points (dash-dotted black lines) are compared to temperatures obtained from the finite-element analysis (solid black lines) and Galerkin's method (dashed black lines) are shown in Figure 8. As it can be seen, despite the inaccuracy of the reduced order model, estimated temperature asymptotically converges to the actual temperature. The deviation of the Galerkin's method from

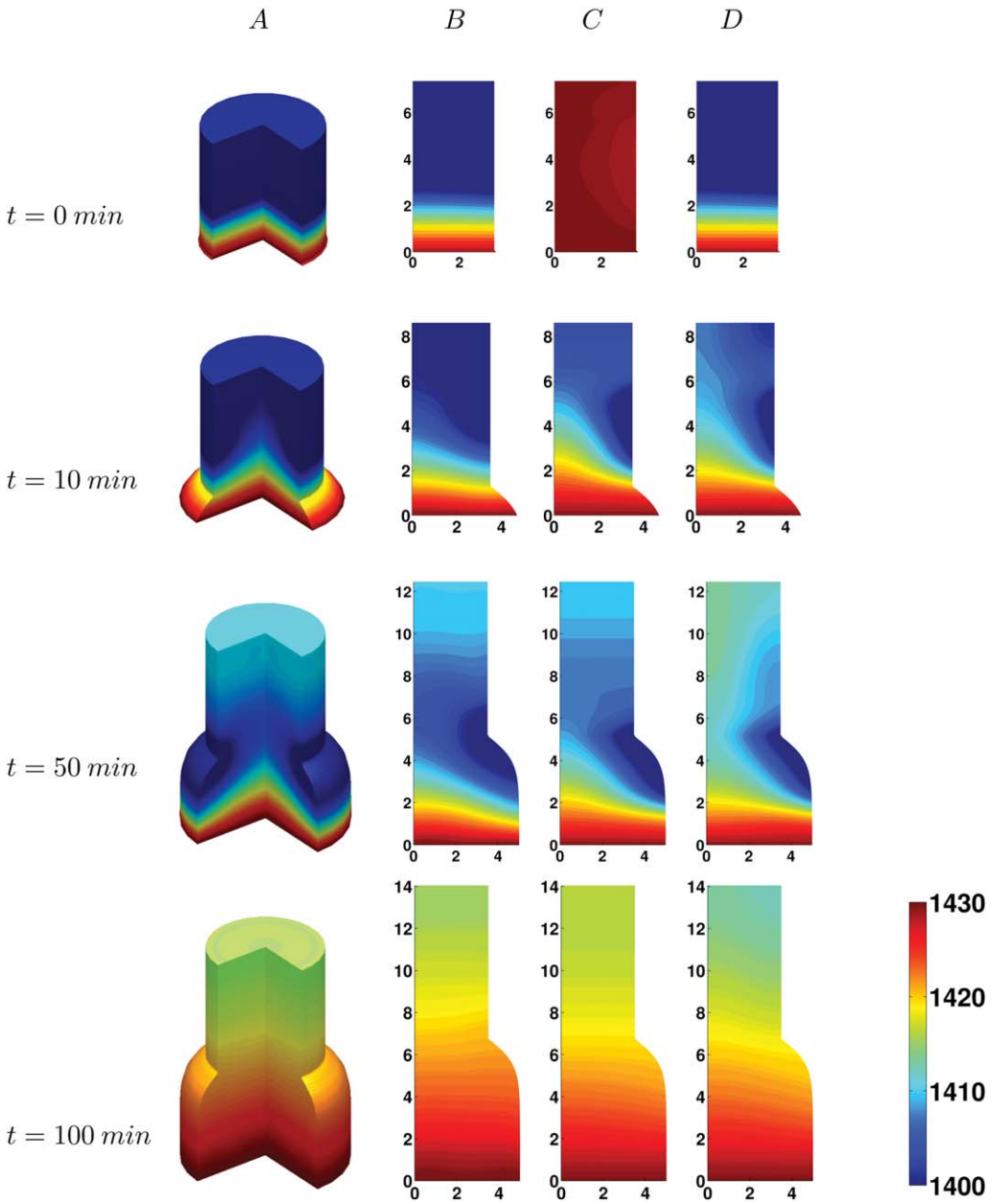

Figure 9. Snapshots at different time instances (t=0; 10, 50, and 100 min), Column A: 3-D FE simulation of the temperature distribution evolution in the crystal; B: 2-D FEM results; C: Reconstructed temperature distribution; D: Open loop Galerkin's method numerical simulation for comparison with FEM.

Note that the initial temperature distribution is not known for the observer at time zero.

FEM is due to the present geometric uncertainty in the crystal domain.

The observer performance is evaluated in the case of a model-plant mismatch. The crystal radius used for observer design and the reduced order Galerkin's model are assumed to be different than the finite-element numerical model realization. Two cases of -20 and $+20\%$ mismatch between radiuses in the observer and the plant are considered and the temperature estimation results are shown in Figure 8. The black lines represent the case with no mismatch while red lines represent $+20\%$ mismatch (radius in observer is greater than the actual value) and blue lines represent the -20% mismatch. The reduced order Galerkin model's result and the estimated temperature are shown by dashed and dash-dotted lines, respectively. Figure 8 shows the estimation performance for both cases. As it can be seen the estimation is more accurate, when a smaller crystal radius is considered in the observer design. This is due to the geometric uncertainty in the crystal shape which is assumed to be rectangular and considering smaller radius for the observer, slightly compensates for this geometric uncertainty and results in a better estimation.

The contour plots of the temperature distribution in the crystal at different time instances are shown in Figure 9. Column A shows the 3-D crystal shape along with the crystal radius evolution as the performance of the radius regulation and the temperature distribution. Column B, C, and D show the FEM results, estimated temperature and the

Galerkin's method simulation results, respectively. At $t = 0$, the temperature distribution in the crystal is unknown and an arbitrary initial condition is assumed for the observer. As it can be seen, the estimated temperature profile (Column C) captures the temperature evolution of the FEM model (Column B). There is a deviation of the results between FEM and Galerkin's method (Column B and D, respectively) which is due to the uncertainties in the modeling, however the estimated temperature distribution shows high degree of agreement with the FEM results.

Conclusions

The coupled model of crystal growth and temperature distribution evolution in the Cz crystallization process is provided to describe the radius and temperature evolution in a time-varying domain. The computational framework of the Galerkin's method is implemented for order reduction and consequently for a low dimensional observer synthesis. The parametric uncertainty in the crystal growth dynamics and geometric uncertainty in parabolic PDE of heat conduction are taken into account in the synthesis of the radius regulation and estimation of temperature distribution in the growing crystal. The observer utilizes boundary temperature measurement to reconstruct the crystal temperature distribution over the entire domain and finally, the obtained reduced order model and the observer is implemented and validated on a numerically realized finite-element model of the Cz crystal growth process. The achieved results show that despite a parametric uncertainty in the crystal growth rate, the geometrical uncertainty in the modeling, time-varying parameters and domain, the reduced order model can be utilized to reconstruct temperature distribution over the entire crystal domain.

Since the temperature gradients during the crystallization process have a significant impact on the grown crystal quality, the reconstructed temperature distribution over the entire crystal domain can be used as a soft sensor for crystal quality monitoring purposes. Moreover, to synthesize a temperature regulation or output feedback controller, the on-line knowledge of the temperature distribution is necessary. The developed framework can be utilized as estimation algorithm along with an output tracking control framework to track a desired temperature distribution profile to guarantee the process stability and crystal quality during the crystallization process.

Acknowledgment

The authors would like to thank Professor Warren Seider and anonymous reviewers for their constructive comments and suggestions.

Notation

α_0 = capillary angle
α_c = growth angle
Δ = matrix of time-varying effects in eigenvalues
ΔH = latent heat
ϵ = ratio corresponding to uncertainty in crystallization rate
Λ = matrix of eigenvalues
λ_{mn} = eigenvalues of the heat equation
Φ_l = heat flux at the interface in the melt
Φ_s = heat flux at the interface in the solid crystal
Φ_{mn} = eigenfunction of the heat equation
ρ_c = crystal density
ρ_l = liquid silicon density
a = Laplace constant
$b(r, z, t)$ = boundary actuation transformation
C_p = heat capacity
C_{growth} = volumetric growth rate
D = bound on the crystallization uncertainty
d = uncertainty in volumetric crystallization rate
$f(z, t)$ = actuation profile
F_{ext} = External pulling force
$F_{\text{Y.L.}}$ = Young–Laplace force
g = gravitational constant
h = total height of crystal from bottom of crucible
h_1 = melt height in crucible
h_2 = total length of
K = control gain
$k_0 = 1/Pe$
k_r = relative thermal conductivity
k_s = regional thermal conductivity
l = crystal length
M_c = crystal mass
p = ransformed temperature distribution
p^e = extended states of the heat equation
Pe = Peclet number
Q = heater input
R_c = crystal radius as a function of crystal length
R_d = reference crystal radius
$R_{\text{c.i.}}$ = crystal radius at the interface
$R_{\text{cruc.}}$ = crucible radius
$u_{\text{mech.}}$ = mechanical input
$u_{\text{th.}}$ = thermal input
v_0 = nominal growth velocity
V_c = crystal volume
v_c = average crystal velocity
V_l = liquid volume
V_m = meniscus volume
V_t = total solid and molten silicon volume
V_z = crystal pulling rate
V_{c0} = initial crystal volume
x = temperature distribution
x_1 = crystal length
x_2 = growth velocity
x_3 = crystal volume
z_1 = heater location, bottom
z_2 = heater location, top

Literature Cited

1. Derby J, Brown R. On the dynamics of Czochralski crystal growth. *J Cryst Growth*. 1987;83(10):137–151.
2. Szabo G. Thermal strain during Czochralski crystal growth. *J Cryst Growth*. 1985;73:131–141.
3. Gevelber M, Stephanopoulos G. Dynamics and control of the Czochralski process. I. Modelling and dynamic characterization. *J Cryst Growth*. 1987;84(4):647–668.
4. Brown R. Theory of transport processes in single crystal growth from the melt. *AIChE J*. 1988;34:881–911.
5. Winkler J, Neubert M, Rudolph J. Nonlinear model-based control of the Czochralski process I: Motivation, modeling and feedback controller design. *J Cryst Growth*. 2010;312:1005–1018.
6. Derby J, Brown R. Thermal-capillary analysis of Czochralski and liquid encapsulated Czochralski crystal growth: I. Simulation. *J Cryst Growth*. 1986;74:605–624.
7. Derby J, Brown R. Thermal-capillary analysis of Czochralski and liquid encapsulated Czochralski crystal growth: II. Processing strategies. *J Cryst Growth*. 1986;75:227–240.
8. Cao J, Gao Y, Chen Y, Zhang G, Qiu M. Simulation aided hot zone design for faster growth of CZ silicon mono crystals. *Rare Metals*. 2011;30(2):155–159.
9. Demina S, Kalaev V. 3D unsteady computer modeling of industrial scale Ky and Cz sapphire crystal growth. *J Cryst Growth*. 2011; 320(1):23–27.
10. Irizarry-Rivera R, Seider WD. Model-predictive control of the Czochralski crystallization process. Part I. Conduction-dominated melt. *J Cryst Growth*. 1997;178(4):593–611.
11. Irizarry-Rivera R, Seider WD. Model-predictive control of the Czochralski crystallization process. Part II. Reduced-order convection model. *J Cryst Growth*. 1997;178(4):612–633.

12. Ng J, Dubljevic S. Optimal boundary control of a diffusion-convection-reaction PDE model with time-dependent spatial domain: Czochralski crystal growth process. *Chem Eng Sci*. 2012;67:111–119.
13. Ng J, Aksikas I, Dubljevic S. Control of parabolic PDEs with time-varying spatial domain: Czochralski crystal growth process. *Int J Control*. 2013;86(9):1467–1478.
14. Armaou A, Christofides P. Crystal temperature control in Czochralski crystal growth process. *AIChE J*. 2001;47(1):79–106.
15. Gevelber M, Stephanopoulos G, Wargo M. Dynamics and control of the Czochralski process II. Objectives and control structure design. *J Cryst Growth*. 1988;91(1–2):199–217.
16. Curtain RF, Zwart H. *An Introduction to Infinite-Dimensional Linear Systems Theory, Texts In Applied Mathematics*. New York: Springer, 1995.
17. Bensoussan A, Prato G, Delfour M, Mitter S. *Representation and Control of Infnite Dimensional Systems*. Boston: Springer, 2007.
18. Krstic M, Smyshlyaev A. *Boundary Control of PDEs: A Course on Backstepping Designs*. Philadelphia: SIAM, 2008.
19. Ito K. Finite-dimensional compensators for innite-dimensional systems via Galerkin-type approximation. *SIAM J Control Optim*. 1990; 28:1251–1269.
20. Fard MP, Sagatun SI. Exponential stabilization of a transversely vibrating beam by boundary control via Lyapunovs direct method. *J Dyn Syst Meas Control*. 2001;123:195–200.
21. Dunbar WB, Petit N, Rouchon P, Martin P. Boundary Control for a Nonlinear Stefan Problem. In: Proceedings of the 42nd IEEE Conference on Decision and Control, 2003:1309–1314.
22. Rudolph J, Winkler J, Woittennek F. Flatness based approach to a heat conduction problem in a crystal growth process. In: Meurer T, Graichen K, Gilles ED, editors. *Control and Observer Design for Nonlinear Finite and Infinite Dimensional System*, Springer Verlag, 2005:387–401.
23. Balas MJ. Finite-dimensional control of distributed parameter systems by Galerkin approximation of infinite dimensional controllers. *J Math Anal Appl*. 1986;114:17–36.
24. Liu WJ, Krstic M. Backstepping boundary control of Burgers' equation with actuator dynamics. *Syst Control Lett*. 2000;41:291–303.
25. Xu CZ, Ligarius P, Gauthier JP. An observer for infinite-dimensional dissipative bilinear systems. *Comput Math Appl*. 1995; 29(7):13–21.
26. Vries D, Keesman KJ, Zwart H. Luenberger boundary observer synthesis for Sturm-Liouville systems. *Int J Control*. 2010;83(7):1504–1514.
27. Li X, Xu C. Infinite-dimensional Luenberger-like observers for a rotating body-beam system. *Syst Control Lett*. 2011;60(2):138–145.
28. Harkort C, Deutscher J. Finite-dimensional observer-based control of linear distributed parameter systems using cascaded output observers. *Int J Control*. 2011;84(1):107–122.
29. Hagen G, Mezic I. Spillover stabilization in finite-dimensional control and observer design for dissipative evolution equations. *SIAM J Control Optim*. 2003;42(2):746–768.
30. Armaou A, Christofides PD. Robust control of parabolic PDE systems with time-dependent spatial domains. *Automatica*. 2001;37:61–69.
31. Wang P. Stabilization and control of distributed systems with time-dependent spatial domains. *J Optim Theory Appl*. 1990;65:331–362.
32. Wang P. Feedback control of a heat diffusion system with time-dependent spatial domains. *Optim Control Appl Methods*. 1995;16: 305–320.
33. Ng J, Dubljevic S. Optimal control of convection-diffusion process with time-varying spatial domain: Czochralski crystal growth. *J Process Control*. 2011;21:1361–1369.
34. Gross U, Kersten R. Automatic crystal pulling with optical diameter control using a laser beam. *J Cryst Growth*. 1972;14:85–88.
35. Jordan A, Caruso R, von Neida A. Analysis of the derivative weight-gain signal from measured crystal shape: implications for diameter control of GaAs. *Bell Syst Tech J*. 1983;62:477–498.
36. Winkler J, Neubert M, Rudolph J. Nonlinear model-based control of the Czochralski process II: reconstruction of crystal radius and growth rate from the weighing signal. *J Cryst Growth*. 2010;312: 1019–1028.
37. Neubert M, Winkler J. Nonlinear model-based control of the Czochralski process III: Proper choice of manipulated variables and controller parameter scheduling. *J Cryst Growth*. 2012;360(1):3–11.
38. Sinno T, Brown R. Modeling microdefect formation in Czochralski silicon. *J Electrochem Soc*. 1999;146(6):2300–2312.
39. Ng J, Aksikas I, Dubljevic S. Application of Optimal Boundary Control to Reaction-Diffusion System with time-varying spatial domain. In: American Control Conference (ACC), *2011*, San Francisco, CA, 2011:2528–2533.
40. Thomas P, Derby J, Atherton L, Brown R, Wargo M. Dynamics of liquid-encapsulated czochralski growth of gallium arsenide: Comparing model with experiment. *J Cryst Growth*. 1989;96(1):135–152.
41. Derby J, Atherton L, Thomas P, Brown R. Finite-element methods for analysis of the dynamics and control of Czochralski crystal growth. *J Sci Comput*. 1987;2(4):297–343.
42. Derby J, Atherton L, Gresho P. An integrated process model for the growth of oxide crystals by the Czochralski method. *J Cryst Growth*. 1989;97(3–4):792–826.
43. Sackinger PA, Brown RA, Derby JJ. A finite element method for analysis of fluid flow, heat transfer and free interfaces in Czochralski crystal growth. *Int J Numer Methods Fluids*. 1989;9(4):453–492.
44. Gevelber M. Dynamics and control of the Czochralski process III. Interface dynamics and control requirements. *J Cryst Growth*. 1994; 139(3–4):271–285.
45. Gevelber M. Dynamics and control of the Czochralski process IV. Control structure design for interface shape control and performance evaluation. *J Cryst Growth*. 1994;139(3–4):286–301.
46. Abdollahi J, Dubljevic S. Crystal Radius and Temperature regulation in Czochralski Crystallization Process. In: American Control Conference (ACC), Washington, DC, 2013:1626–1632.
47. Duffar T. *Crystal Growth Processes Based on Capillarity: Czochralski, Floating Zone, Shaping and Crucible Techniques*. U.K.: Wiley, 2010.
48. Reddy JN. *An Introduction to Nonlinear Finite Element Analysis*. Oxford: Oxford University Press, 2004.
49. Ray WH. *Advanced process control*. McGraw-Hill chemical engineering series. New York: McGraw-Hill, 1981.
50. Izadi M, Dubljevic S. Order-reduction of parabolic PDEs with time-varying domain using empirical eigenfunctions. *AIChE J*. 2013;59: 4142–4150.

Manuscript received Sept. 9, 2013, and revision received Apr. 28, 2014.